


Geometric description for the anatomy of the mitral valve: A review

Diana Oliveira¹  | Janaki Srinivasan² | Daniel Espino¹ | Keith Buchan³ | Dana Dawson⁴ | Duncan Shepherd¹

¹Department of Mechanical Engineering, University of Birmingham, Birmingham, UK

²Cardiac Department, Aberdeen Royal Infirmary, Aberdeen, UK

³Department of Cardiothoracic Surgery, Aberdeen Royal Infirmary, Aberdeen, UK

⁴Cardiology Research Facility, University of Aberdeen and Aberdeen Royal Infirmary, Aberdeen, UK

Correspondence

Diana Oliveira, Department of Mechanical Engineering, University of Birmingham, Edgbaston, Birmingham B15 2TT, UK. Email: DMC795@student.bham.ac.uk

Funding information

The creation of the database employed in our study was sponsored by the University of Aberdeen, under the research study 'Exercise Capacity in Adults'.

Abstract

The mitral valve is a complex anatomical structure whose physiological functioning relies on the biomechanical properties and structural integrity of its components. Their compromise can lead to mitral valve dysfunction, associated with morbidity and mortality. Therefore, a review on the morphometry of the mitral valve is crucial, more specifically on the importance of valve dimensions and shape for its function. This review initially provides a brief background on the anatomy and physiology of the mitral valve, followed by an analysis of the morphological information available. A characterisation of mathematical descriptions of several parts of the valve is performed and the impact of different dimensions and shape changes in disease is then outlined. Finally, a section regarding future directions and recommendations for the use of morphometric information in clinical analysis of the mitral valve is presented.

KEYWORDS

biomechanics, computational anatomy, mitral valve, mitral valve disease, morphology analysis

1 | INTRODUCTION

The mitral valve (MV) is one of the heart's four valves, lying between the left atrium and the left ventricle. It prevents blood from flowing backwards as it moves through the heart and it has a complex geometry, comprising the mitral annulus, the anterior and posterior leaflets, and the subvalvular apparatus (Figure 1). The latter is formed by the chordae tendineae and the papillary muscles (PM), which are inserted into the left ventricular wall (McCarthy *et al.*, 2010; Dal-Bianco and Levine, 2013). These structures work in synchrony towards its effective mechanics to enable closing and opening through the cardiac cycle (McCarthy *et al.*, 2010).

The shape of the valve is key to many aspects of its function and disease, as identified by clinical studies (Lee *et al.*, 2013; Jassar *et al.*, 2014) as well as silico studies, based on porcine (Kunzelman *et al.*, 2007), ovine (Eckert *et al.*, 2009) and human (Stevanella *et al.*, 2011) models, and in vitro studies, based on porcine (Espino *et al.*, 2007) and ovine (Bloodworth *et al.*, 2017) models. Assessing its morphology can reveal various normal and abnormal features, which can be

associated with deteriorating clinical outcomes (Sonne *et al.*, 2009; Lee *et al.*, 2013; Mihaila *et al.*, 2013; Jolley *et al.*, 2017). Moreover, the physiological functioning of the components of the MV, as well as their ability to adapt to altered stress state imposed by the passage of blood flow, relies on their biomechanical properties and structural integrity (Espino *et al.*, 2007; Al-Atabi *et al.*, 2012). The success of surgical interventions (such as edge-to-edge repair or chordal replacement; Al-Atabi *et al.*, 2012) greatly depends on the restoration of normal fluid dynamics, which typically requires valve mechanics to be corrected (Al-Atabi *et al.*, 2012). Thus, optimising a surgical procedure, or surgical timing for MV repair, is arduous (Gao *et al.*, 2017b). The design of medical devices for the MV is also determined by its morphometry, with a previous in vitro study based on porcine MVs supporting the use of saddle-shaped annuloplasty ring designs to better mimic annular shape (Jimenez *et al.*, 2007).

The first study reviewing the anatomic structure of the MV to identify key dimensions appeared at the beginning of the 1990s and was based on excised human and porcine MV apparatus (Kunzelman *et al.*, 1994). This yielded basic human and porcine MV

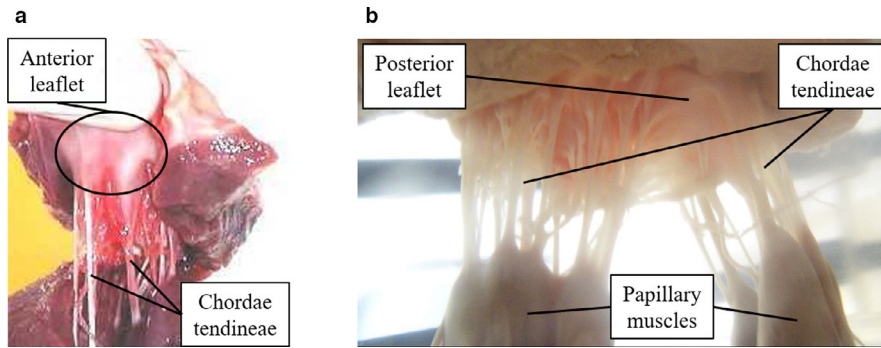


FIGURE 1 Porcine mitral valve apparatus: (a) displays the anterior leaflet and chordae tendineae and (b) focuses on the subvalvular apparatus, where chordae arise from both PMs and insert into the rough region of the posterior leaflet

ex vivo measurements concerning annular and leaflet length and height, and chordal distribution. With the evolution of medical imaging modalities, in vivo procedures, such as three-dimensional (3D) transoesophageal echocardiography, have been used quantitatively to evaluate human MV morphology in healthy and diseased cases (Sonne *et al.*, 2009; Delgado *et al.*, 2009; Lee *et al.*, 2013; Mihaila *et al.*, 2013; Jolley *et al.*, 2017), proving crucial for 3D printing purposes or transcatheter MV implantation, for example. On the other hand, computational studies have mathematically represented the MV (Salgo *et al.*, 2002; Stevanella *et al.*, 2009; Park *et al.*, 2019), including the annulus (Salgo *et al.*, 2002; Stevanella *et al.*, 2009), leaflet shape (Stevanella *et al.*, 2009; Shen *et al.*, 2017; Park *et al.*, 2019) and chordae architecture (Kaiser *et al.*, 2019) from both human and porcine dimensions and characteristics. Although many sources of MV anatomy quantification exist, a single study bringing together the current best knowledge around its morphometry, including related mathematical definitions, is lacking.

This review article aims to examine the morphometry of the MV and determine the current state of mathematical definitions of its geometrical shape. The focus is on compiling ex vivo/in vivo descriptions which are currently available in the literature to define the 3D geometry of the MV. The anatomy and physiology of the MV are briefly described, followed by mathematical definitions and morphometric information available (including associations between valve dimensions). Subsequently, a description of the impact of changes in MV morphometry in valve disease is performed and future recommendations for the use of morphometric information in MV clinical analysis are given.

2 | ANATOMY AND PHYSIOLOGY OF THE MITRAL VALVE

2.1 | Mitral annulus and leaflets

The annulus is a ring of fibrous tissue that circumscribes the perimeter of the valvular orifice and the base of the valve, anchoring it within the left heart (Dal-Bianco and Levine, 2013). It is adjacent to the aortic valve, sharing a fibrous continuity with the left coronary and half of the non-coronary cusps of the aortic annulus (Ranganathan *et al.*, 1970; Veronesi *et al.*, 2009). This adjacent section defines the anterior portion of the mitral annulus, limited by the left and right fibrous

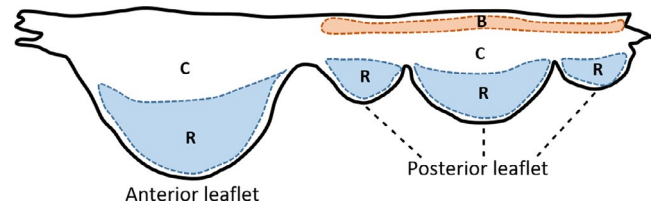


FIGURE 2 Human MV leaflet tissue areas. C, clear zone; R, rough zone; B, basal zone

trigones. The posterior part of the annulus is distal to the trigones and includes the lower points of its saddle shape (Dal-Bianco and Levine, 2013). Its shape and diameter vary during the cardiac cycle (Jiang *et al.*, 2014), making it a dynamic structure: in diastole, the annulus has a more circular shape, whereas in systole it changes into a non-planar saddle shape in synchrony with valve closure/leaflet coaptation (Al-Atabi *et al.*, 2012; Dal-Bianco and Levine, 2013; Garbi and Monaghan, 2015).

The leaflets of the MV are a continuous band of tissue extending from the annulus. According to their geometrical form and anatomical connection to the annulus, the leaflets are divided into anterior, posterior and commissural parts (McCarthy *et al.*, 2010; Dal-Bianco and Levine, 2013). According to previous studies focusing on the human MV, the posterior leaflet has a semilunar shape and a relatively short radial length in comparison with the anterior leaflet, being composed of three minor semi-oval scallops: a central one opposite to the anterior leaflet, and two others, to each side (Ranganathan *et al.*, 1970; Carpentier *et al.*, 1995; Dal-Bianco and Levine, 2013). The anterior leaflet, on the other hand, is dome-shaped, longer and thicker (Ranganathan *et al.*, 1970; Dal-Bianco and Levine, 2013). In systole, the free edge of both leaflets coapt, closing the valve (Ranganathan *et al.*, 1970), whereas in diastole, the free edges separate and the valve opens (McCarthy *et al.*, 2010). Tissue characteristics of both leaflets also change according to region, as stated by previous human mitral valve studies and as displayed in Figure 2: while the central portion is thinner and smoother (clear zone), towards the free edges (coaptation region) the tissue becomes thicker and rougher (rough zone) (McCarthy *et al.*, 2010; Al-Atabi *et al.*, 2012; Dal-Bianco and Levine, 2013); this is the main area of chordae tendineae attachment (Lam *et al.*, 1970; Dal-Bianco and Levine, 2013). The posterior leaflet also possesses a chordae attachment area near the annulus, named the basal zone (Lam *et al.*, 1970). Both leaflets consist of four histological layers. The uppermost one

adjacent to the left atrium is the atrialis, composed of mainly aligned elastic/collagen fibres. Beneath the atrialis is the spongiosa, which consists of an extracellular matrix of proteoglycans and glycosaminoglycans, along with elastic fibres, comprising the majority of the free edge. Beneath the spongiosa is the fibrosa, a major load-bearing layer forming the central structural collagenous core of each leaflet, with aligned collagen fibres. Finally, the ventricularis layer is covered by a continuous sheet of endothelial cells folded with elastic and collagen fibres (McCarthy *et al.*, 2010).

2.2 | Subvalvular apparatus

The chordae are chord-like structures that arise from the tip of either of the two PMs and insert into the leaflets (Lam *et al.*, 1970; Al-Atabi *et al.*, 2012). The two PMs are known as anterolateral and posteromedial, relative to the anterior and lateral body orientations and indicating the anatomical parts of the left ventricular wall into which they insert. Similarly to the mitral annulus, they are dynamic structures that move through the cardiac cycle. However, their role is unclear in the literature: previous studies focusing on dog mitral valves state that PM contraction/shortening assists in opening the MV, whereas their elongation aids in coaptation (Marzilli *et al.*, 1980), or that MV closing relies on PM contraction instead (Hirakawa *et al.*, 1977). The chordae themselves are characterised according to their point of attachment and size; in a human MV, the marginal chordae are thinnest and attach to the free edge of the leaflets; basal chordae are thicker and more extensible, inserting between the free edges and the leaflet's attachment to the annulus (rough zone).

There are two thick basal chords (strut chordae) that arise from the tip of each PM and insert into the anterior leaflet: these are

the largest and thickest of all chordae, having also the highest tension (Lam *et al.*, 1970; Lomholt *et al.*, 2002; Al-Atabi *et al.*, 2012; Dal-Bianco and Levine, 2013; Wilcox *et al.*, 2014). Their insertion region into the anterior leaflet experiences varying stretch during the cardiac cycle, which demonstrates a transfer of forces from the leaflets to the chordae and vice versa, and aids in valve function (Padala *et al.*, 2010). There are also tertiary chordae, which originate at the left ventricular wall and connect to the basal region of the posterior leaflet (McCarthy *et al.*, 2010; Al-Atabi *et al.*, 2012). According to porcine and ovine studies, different types of chordae have different functions: whereas marginal chordae maintain the leaflets closed during systole, averting regurgitation, basal chordae support and transfer loads to the leaflets, carrying also higher loads to protect marginal chordae from failure (Timek *et al.*, 2001; Sedransk *et al.*, 2002; Nielsen *et al.*, 2003; Espino *et al.*, 2005; Wilcox *et al.*, 2014).

3 | INSIGHTS INTO MITRAL VALVE MORPHOMETRY

3.1 | Mitral valve key landmarks and morphometric data

Mathematical algorithms that automatically generate parametric 3D human MV models have been developed from in vivo echocardiographic data (Grbic *et al.*, 2017), four-dimensional computed tomography images (Ionasec *et al.*, 2010) and 3D transoesophageal echocardiography (Mansi *et al.*, 2012; Zhang *et al.*, 2017). Despite the creation of patient-specific geometries, these frameworks rely on common anatomic MV landmarks (Figure 3), from which parametric surfaces corresponding to the mitral leaflets can be generated.

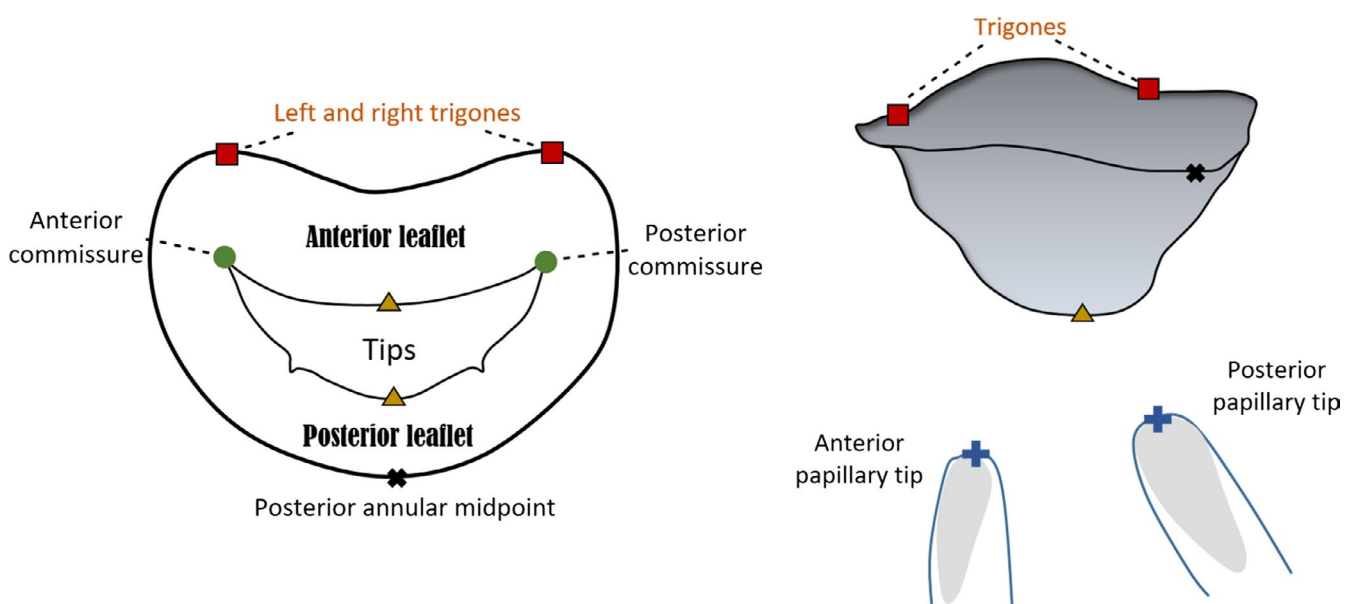


FIGURE 3 Atrial and lateral views of a mitral valve (MV) schematic model based upon nine landmarks. The annulus, anterior and posterior leaflets and papillary muscle tips can be observed

TABLE 1 Geometric variables of the MV and healthy and diseased (significant regurgitation) literature ranges (Ranganathan *et al.*, 1970; Kunzelman *et al.*, 1994; Yamaura *et al.*, 2008; Delgado *et al.*, 2009; Sonne *et al.*, 2009; Suri *et al.*, 2009; Lee *et al.*, 2013; Mihaila *et al.*, 2013; Topilsky *et al.*, 2013; Dudzinski and Hung, 2014; Jassar *et al.*, 2014; Jiang *et al.*, 2014; Kim *et al.*, 2014; Pouch *et al.*, 2014; Calleja *et al.*, 2015; Machino-Ohtsuka *et al.*, 2016; Obase *et al.*, 2016; Owais *et al.*, 2016; Deorsola and Bellone, 2018)

MV component	Geometric variables	Meaning	Ranges	
			Healthy	Diseased
Annulus	AP diameter (mm)	Distance between anterior and posterior annular midpoints	30 ± 6 ^b	38.8 ± 6.4 ^c
	CW (mm)	Annular diameter at the commissures	33.3 ± 3.7 ^c	42.2 ± 5.9 ^c
	AL-PM diameter (mm)	Diameter between anterolateral and posteromedial landmarks	31 ± 5 ^b	39 ± 7 ^b
	Annular circumference (mm)	Total perimeter of the annular edge	106 ± 10 ^c	136 ± 19 ^c
	Anterior/posterior circumferences (mm)	Perimeter of the anterior/posterior annular edges	Anterior: 43.3 ± 8.2 ^b Posterior: 63.01 ± 9.06 ^b	Anterior: 61.3 ± 8 ^b Posterior: 75 ± 11 ^b
	Annular height (mm)	Vertical distance between highest and lowest annular points	7.9 ± 1.9 ^c	5.6 ± 1.6 ^c
	Annular area (mm ²)	Area enclosed by the 2D projection of the annulus	780 ± 270 ^b	1,343 ± 392 ^c
	NPA (°)	Angle between anterior and posterior annular midpoints at the commissure	144 ± 11 ^b	157 ± 12 ^b
	IT distance (mm)	Distance between left and right trigones	30 ± 3 ^d	31 ± 3 ^d
Leaflets	Anterior/posterior lengths (mm)	Length from anterior/posterior annular midpoints to coaptation	Anterior: 21.2 ± 3.0 ^c Posterior: 9.8 ± 2.0 ^c	Anterior: 26.3 ± 6.1 ^c Posterior: 16 ± 5 ^c
	Anterior/posterior areas (mm ²)	Surface area of anterior/posterior leaflets	Anterior: 530 ± 210 ^b Posterior: 380 ± 130 ^b	Anterior: 760 ± 190 ^b Posterior: 610 ± 230 ^b
	Posterior scallop lengths (mm)	Length from each scallop free margin to annulus	P1: 5-17; P2: 7-20; P3: 7-20 ^e	P1: 16 ± 5; P2: 19 ± 6; P3: 16 ± 4 ^b
	Commissural heights (mm)	Height from each commissural free margin to annulus	AL: 5-13; PM: 4-12 ^e	-----
	Leaflet angles (°)	Angle created by the anterior/posterior leaflets with the annulus line	Anterior: 24.6 ± 7 ^b Posterior: 34.7 ± 9.6 ^b	Anterior: 33.2 ± 8.6 ^b Posterior: 44.4 ± 11.9 ^b
	Tenting height (mm)	Distance from the annulus to coaptation	7.4 ± 1.3 ^a	9.7 ± 3.2 ^b
	Tenting area (mm ²)	Silhouette delineated by leaflets from annulus to coaptation	118.2 ± 32.6 ^a	350 ± 50 ^a
Subvalvular apparatus	PM length (mm)	Length from each PM to anterior annular midpoint	ALPM: 28.1 ± 4.1 ^c PMPM: 28.5 ± 4.8 ^c	ALPM: 40.5 ± 6 ^c PMPM: 41.8 ± 5.9 ^c
	Inter-papillary distance (mm)	Distance between PMs	Inner: 14.4 ± 4.8 ^b Outer: 31.1 ± 5.4 ^b	Inner: 26.7 ± 8.4 ^b Outer: 43.1 ± 9.7 ^b
	Inter-papillary angle (°)	Angle between anterior annular midpoint to both PMs	26.2 ± 6.5 ^d	28.9 ± 6.3 ^d

Note: Dimensions obtained at: a, early systole; b, mid-systole; c, end-systole; d, averaged over cardiac cycle; e, ex vivo.

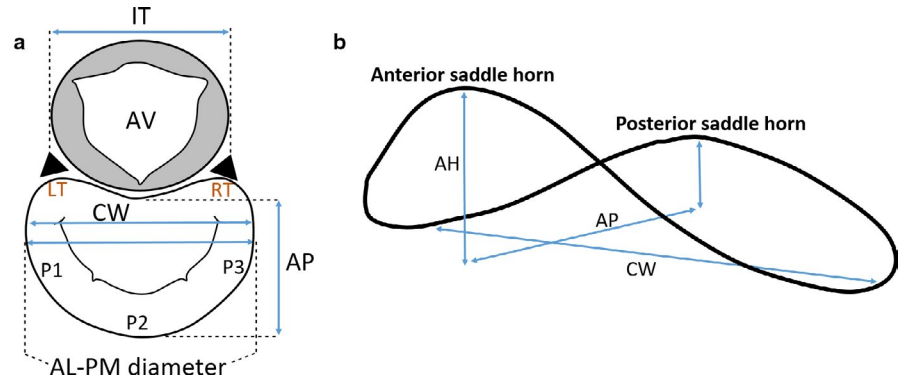
AL, anterolateral; ALPM, anterolateral papillary muscle; AL-PM, anterolateral-posteromedial; AP, antero-posterior; CW, commissural width; IT, inter-trigonal; NPA, non-planarity angle; P1, posteromedial commissural scallop; P2, posterior middle scallop; P3, anterolateral commissural posterior scallop; PM, papillary muscle; PMPM, posteromedial papillary muscle.

These include the left and right trigones, situated at the fibrous border between the mitral and aortic valves (Veronesi *et al.*, 2009); the anterolateral and posteromedial commissures, located at the free edges, which are the interconnection points of the leaflets (McCarthy *et al.*, 2010); the leaflet tips, corresponding to the line of each leaflet free edge (Ionasec *et al.*, 2010; Mansi *et al.*, 2012); the

posterior annular midpoint; and the PM tips (Ionasec *et al.*, 2010; Mansi *et al.*, 2012).

Both ex vivo and in vivo studies defined parameters that describe the human MV geometrical shape and are vital to its function. These are discretised in Table 1, and ranges of values for healthy and diseased valves are provided.

FIGURE 4 Atrial (a) and lateral (b) views of important mitral annular dimensions. AV, aortic valve; LT, left trigone; RT, right trigone; P1, P2, P3, posterior leaflet scallops; AL-PM diameter, anterolateral-posteromedial diameter; AP, antero-posterior distance; CW, commissural width; IT, inter-trigonal distance



3.2 | Annular proportions and saddle shape: geometrical relationships

The geometrical components of the annulus including annular anterior and posterior areas, the antero-posterior (AP), the anterolateral-posteromedial (AL-PM) and the inter-trigonal distances, represented in Figure 4a, vary over the cardiac cycle (Jiang *et al.*, 2014). Both anterior and posterior annular portions contribute to changes in mitral annular area: although standard literature refers to annular contraction as occurring during systole, as stated in a previous ovine study (Rausch *et al.*, 2011), there are studies based on human MVs showing annular expansion from mid-systole to early-diastole and contraction between mid-diastole and early systole (Levack *et al.*, 2012; Jiang *et al.*, 2014). In addition, an *in vivo* study based on ovine MVs showed the presence of dynamic annular strain, with the largest strains belonging to the posterior region and the commissural regions showing the least amount of variation (Eckert *et al.*, 2009).

Despite this dynamic variability, the proportion concerning anterior and posterior annular circumferences in the human MV remains practically unchanged. This proportion is contradictory in the literature: whereas some studies mention that the anterior and posterior parts correspond to about 1/3 and 2/3 of the total annular perimeter (Garbi and Monaghan, 2015), others yield a proportionality of about 2/5 and 3/5, respectively (Pouch *et al.*, 2014; Jassar *et al.*, 2014). However, this proportion depends on the assumed division between leaflets, which is usually considered at the commissural level. Nonetheless, other studies divide the leaflets at the lowest annular height. The correct proportion is reflected in the literature values (obtained at mid-systole) present in Table 1 (Pouch *et al.*, 2014; Jassar *et al.*, 2014) and is described quantitatively by Equations (1) and (2),

$$P_{AC} = 3/5 \cdot A_C \quad (1)$$

$$A_{AC} = 2/5 \cdot A_C \quad (2)$$

where A_C is the total annular circumference and P_{AC} and A_{AC} are the posterior and anterior annular circumferences, respectively. Moreover, these proportions are confirmed by correlations found in the literature, based upon dimensional data retrieved during intra-cardiac operations and

dissection of fresh human hearts (Duplessis and Marchand, 1964). These yielded Equation (3) ($R^2 = .72$, p -value < .01) and 4 ($R^2 = .93$, p -value < .01),

$$A_{AC} = 4.137 + 0.305 \cdot A_C \quad (3)$$

where the A_C and A_{AC} are in mm,

$$P_{AC} = -4.137 + 0.695 \cdot A_C \quad (4)$$

where the A_C and P_{AC} are in mm. The correlation from Equation (4) was further validated through a 2D echocardiographic study concerning imaging data from 15 healthy subjects and performed by the authors. Valvar dimensions were obtained at end-systole and generated a moderate correlation between the A_C and P_{AC} ($R^2 = .674$, p -value < .01). The methodology employed for equation prediction generation, as well as further characteristics of the correlations found on our study, are present in Appendix S1.

An *ex vivo* human study, performed within 6 hours of MV removal, examined MV geometry by assuming the mitral annulus as a circle and the A_{AC} and P_{AC} as arc lengths. This work also underlined positive linear relationships between these dimensions and the mitral annular diameter (or AL-PM distance), as given by Equation (5) ($R^2 = .66$, p -value < .01) and 6 ($R^2 = .91$, p -value < .01) (Okamoto *et al.*, 2007):

$$A_{AC} = 2.500 + 0.420 \cdot \gamma \quad (5)$$

where γ represents the AL-PM distance and both variables are in cm,

$$P_{AC} = 4.400 + 1.200 \cdot \gamma \quad (6)$$

where both variables are in cm. For Equations (5) and (6), γ is expressed as a dimensionless Z-value in agreement with Okamoto *et al.* (2007). Further, the authors of this study have mathematically defined the A_{AC} , P_{AC} and IT distance, assuming the annulus as divided into anterior and posterior portions by the left and right trigones or commissures, as represented in Figure 5.

Equations (7)-(9) represent the mathematical definitions employed by Okamoto *et al.* (2007),

$$IT = 2 \cdot \gamma \cdot \sin\left(\frac{\theta_{Tg}}{2}\right) \quad (7)$$

$$A_{AC} = \pi \cdot \gamma \cdot \theta_{Tg} \cdot \theta_{Com}, \quad (8)$$

$$P_{AC} = \pi \cdot \gamma \cdot (360 - \theta_{Tg} \cdot \theta_{Com}) / 360, \quad (9)$$

where IT is the inter-trigonal distance, γ is the AL-PM distance, θ_{Tg} is the angle between left and right trigones and θ_{Com} is the angle between commissures at the annular plane (Okamoto *et al.*, 2007). However, these definitions simplify the shape of the anterior leaflet to great extent and do not accurately represent its real configuration.

An association between the annular circumference and the total leaflet free edge length has also been found based on the *ex vivo* human MV data from Duplessis and Marchand (1964). Greater total and posterior annular circumferences were moderately correlated with increased free edge lengths, as provided in the equations below,

$$\delta = 18.824 + 0.704 \cdot A_C, \quad (10)$$

where δ represents the free edge length, and both variables are in mm ($R^2 = .76$, p -value < .01),

$$\delta = 26.301 + 0.964 \cdot P_{AC}, \quad (11)$$

where both variables are in mm ($R^2 = .74$, p -value < .01),

Annular shape is distinctive due to its similarity with a saddle, being characterised by an annular height (AH) (Figure 4b). This is characteristic of a healthy valve, as it reduces leaflet stress and decreases anterior systolic strain, potentially increasing repair durability (Salgo *et al.*, 2002; Jimenez *et al.*, 2007). In practice, a deeper saddle relates to more apical positions of the medial and lateral aspects of the annulus, while the anterior and posterior aspects remain basal (Salgo *et al.*, 2002). This is mathematically described by the annular height to commissural width ratio (AHCWR), which provides a quantitative measure of annular non-planarity (Lee *et al.*, 2013; Jassar *et al.*, 2014; Pouch *et al.*, 2014). According to this, we can also define the AHCWR as:

$$\varepsilon = AH/AP \cdot CI, \quad (12)$$

where ε represents the AHCWR, AH is the annular height, AP is the antero-posterior distance and CI is the circularity index. The latter is defined as the ratio between the AP diameter and the commissural

width (CW) and accounts for the greater or smaller ellipsoidal shape of the annulus (Lee *et al.*, 2013; Pouch *et al.*, 2014).

The human MV AHCWR profile depends on the rotational position of the annulus and has led to the generation of new annuloplasty ring designs (Jassar *et al.*, 2014; Pouch *et al.*, 2014). In fact, saddle shape variability impacts on leaflet stress variation (Salgo *et al.*, 2002); a deeper saddle shape, associated with a higher AHCWR percentage (Lee *et al.*, 2013), leads to leaflet peak stress reduction, as predicted by computational studies (Salgo *et al.*, 2002). Further, geometrical correlations concerning the AL-PM distance and other mitral annular dimensions have been found both in the literature and in our 2D echocardiographic study. For example, a clinical 3D transoesophageal echocardiography study focusing on the end-systolic frame yielded lower non-planarity angles (NPA) that were associated with increased AH to the AL-PM distance ratios, as given by Equation (13) ($R^2 = .70$, p -value < .01) (Warrach *et al.*, 2012):

$$NPA = 179.600 - 163.900 \cdot \sigma, \quad (13)$$

where σ represents the AH to the AL-PM distance ratio (dimensionless) and the NPA is in degrees. A moderate association between the ratio of the AH to the AL-PM distance and the ratio of the AH to the AP distance was also found ($R^2 = .78$, p -value < .01) (Warrach *et al.*, 2012):

$$\sigma = 0.027 + 0.970 \cdot \tau, \quad (14)$$

where τ represents the AH to the AP distance ratio. Nonetheless, given mitral annular dynamic shape changes through the cardiac cycle (the AH suffers a total percentage change of 13.5 ± 7.8 in the cardiac cycle, for example; Tang *et al.*, 2019), we cannot assume that the aforementioned relationships are maintained both in systole and in diastole.

Our 2D echocardiographic study revealed a moderate association between the AL-PM distance and the inter-trigonal distance at end-systole, displayed in Equation (15) ($R^2 = .65$, p -value < .01):

$$IT = 19.280 \cdot e^{(0.017 \cdot \gamma)} \quad (15)$$

where IT represents the inter-trigonal distance and both variables are in mm.

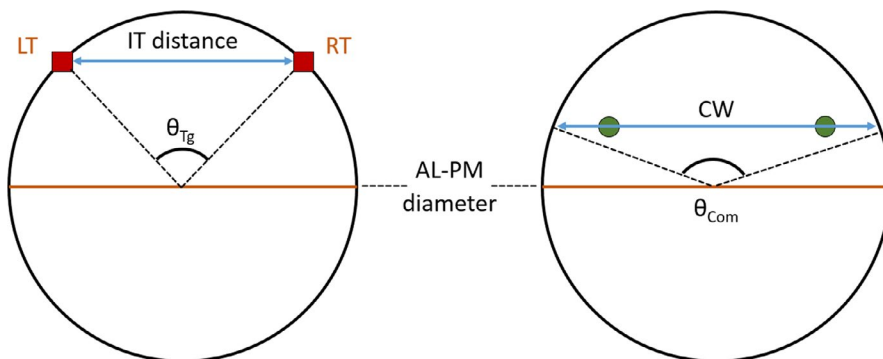


FIGURE 5 Circle representing the annulus, according to Okamoto *et al.* (2007), with relevant dimensions highlighted. LT, left trigone; RT, right trigone; AL-PM diameter, anterolateral-posteromedial diameter; CW, commissural width; IT distance, inter-trigonal distance; θ_{Tg} , trigonal angle; θ_{Com} , commissural angle

The AP distance is also geometrically associated with other annular parameters in the human MV. Equations (16) and (17) present moderate correlations between the ratio of the AH to the AP distance and the NPA ($R^2 = .64$, p -value $< .01$) and between the 2D annular area and the AP distance ($R^2 = .65$, p -value $< .01$), respectively, generated with data obtained at end-systole:

$$\text{NPA} = 177.580 - 142.880 \cdot \tau, \quad (16)$$

where τ is dimensionless and the NPA is in $^\circ$,

$$\text{AP} = 18.206 + 0.016 \cdot A_{\text{na}}, \quad (17)$$

where A_{na} is the annular area in mm^2 and AP is in mm.

The annular saddle shape has been mathematically defined through paraboloid equations, which are quadric surfaces with one axis of symmetry and no centre of symmetry (Salgo *et al.*, 2002; Stevanella *et al.*, 2009; Park *et al.*, 2019). In Salgo *et al.* (2002), for example, hyperbolic paraboloids were employed (Salgo *et al.*, 2002), whereas Park *et al.* used hyperbolic paraboloids for the saddle shape definition. In addition, they designed a ring-shaped structure, mathematically described as a curved toroid and with empirical relationships derived below (Park *et al.*, 2019):

$$z = \frac{(x - \alpha_L)^2}{a \cdot \alpha_V} - \frac{(y - \beta_L)^2}{b \cdot \beta_V}, \quad (18)$$

where α_L and β_L are transformation parameters in lateral directions in the xy plane that define the saddle point, α_V is a transformation parameter in the vertical direction in the xz plane, and β_V is the transformation parameter in the vertical direction in the yz plane. These parameters vary between 0 and 1, and a and b are determined by annular dimensions:

$$a = \frac{(\gamma)^2}{4 \cdot \text{AH}} \quad (19)$$

$$b = \frac{(\text{AP})^2}{4 \cdot \text{AH}} \quad (20)$$

Equation (18) allows the manipulation of lateral and vertical curve transformations representative for example of changes in saddle depth and commissural height (see Figure 6).

The NPA is not the only factor influencing annular saddling; the leaflet angles (α_A , and α_P , represented in Figure 7) and the overall coaptation triangle (2D triangle formed by the AP diameter, anterior and posterior leaflets when the leaflets coapt), including tenting height and tenting area, also play an important role in the evaluation of human MV geometry and function (Delgado *et al.*, 2009; Ciarka *et al.*, 2010; Silbiger, 2011; Deorsola and Bellone, 2018). A schematic of this coaptation triangle is represented in Figure 7, as well as related linear and angular dimensions. A previous study hypothesised that the coaptation triangle of healthy valves could be based on the Golden

Proportion, a ratio observed in Nature which derives from sectioning a certain segment in two different parts (Deorsola and Bellone, 2018). Such ratios yield an irrational number (rounded to .618 or 1.618) known as the Golden Proportion. This study states that the value of .618 can be obtained through the ratio between the anterior cord and the AP diameter, between the posterior and the anterior cords, and between the tenting height and the posterior cord.

Indeed, Deorsola *et al.* found strong correlations between the original coaptation triangle and the Golden (or mathematical) one at early systole (time point of measurements), showing good positive linear relationships between the AP diameter and the anterior cord (Equation 21, $R^2 = .97$, p -value $< .01$) and between anterior and posterior cords (Equation 22, $R^2 = .82$, p -value $< .01$):

$$A_{\text{cord}} = 1.391 + 0.580 \cdot \text{AP}, \quad (21)$$

where the AP diameter and A_{cord} (anterior cord) are in mm,

$$P_{\text{cord}} = -1.279 + 0.667 \cdot A_{\text{cord}}, \quad (22)$$

where the A_{cord} and P_{cord} (posterior cord) are in mm. Unfortunately, Deorsola *et al.* mention that, due to technical imaging limitations, they were unable to assess the coaptation triangle and repeat measurements for each frame of the cardiac cycle in order to determine whether the Golden Proportion or the correlations found would be maintained both in systole and diastole (Deorsola and Bellone, 2018). Nonetheless, the anterior and posterior leaflet angles are an important element for the evaluation of leaflet tethering, with a posterior leaflet angle of $\geq 45^\circ$ being an index of severe leaflet tethering in ischaemic mitral regurgitation. In fact, a previous study found that a P3 tethering angle below 28.8° would predict the improvement of this type of regurgitation after surgery (Bouma and Gorman, 2019; Sun *et al.*, 2019). From a diagnostic and surgical point of view, this means that leaflet angles could represent important parameters to identify early anatomical alterations or to improve surgical strategy and postoperative evaluation, especially when correlated with other MV dimensions of the coaptation triangle (Deorsola and Bellone, 2018).

3.3 | Leaflet dimensions and shape

Figure 8 shows anterior and posterior leaflet heights and lengths, as well as commissural length and leaflet area for a generic human MV.

Geometrical associations concerning the anterior leaflet have been determined from *ex vivo* human data from Duplessis and Marchand (1964). Dependencies between anterior leaflet surface area and other dimensions of the valve were discovered: correlations are present between this area and the A_C (Equation 23, $R^2 = .70$, p -value $< .01$) and A_{AC} (Equation 24, $R^2 = .81$, p -value $< .01$), with a moderate correlation between this area and the free edge lengths (Equation 25, $R^2 = .62$, p -value $< .01$),

$$A_{LA} = 127.300 + 3.549 \cdot A_C, \quad (23)$$

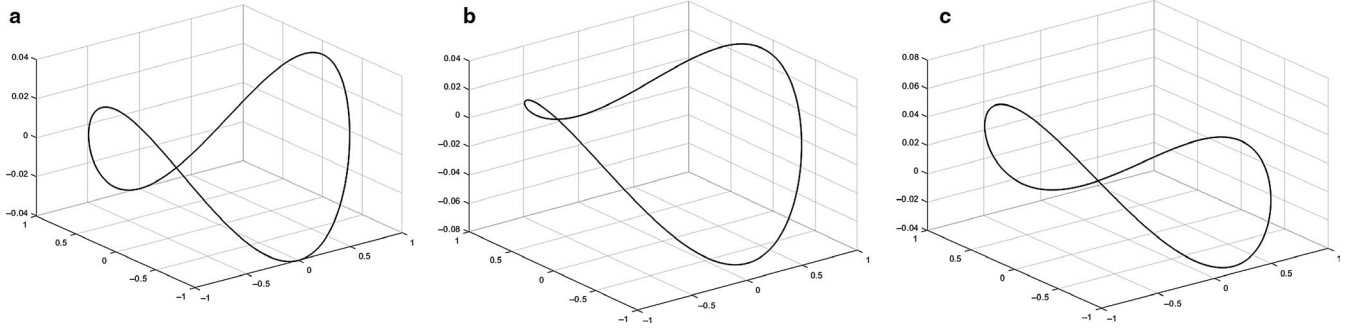


FIGURE 6 Hyperboloids representing the mitral valve (MV) saddle shape and defined by Equation 11 (Park *et al.*, 2019) are displayed, created from literature values for CW (33.3 mm), AP diameter (28 mm), AL-PM diameter (31 mm) and AHCWR (0.237). Different commissural heights (b) and posterior annular depth (c) in comparison with a pure hyperboloid (a) can be observed, shown by changes in transformation parameters

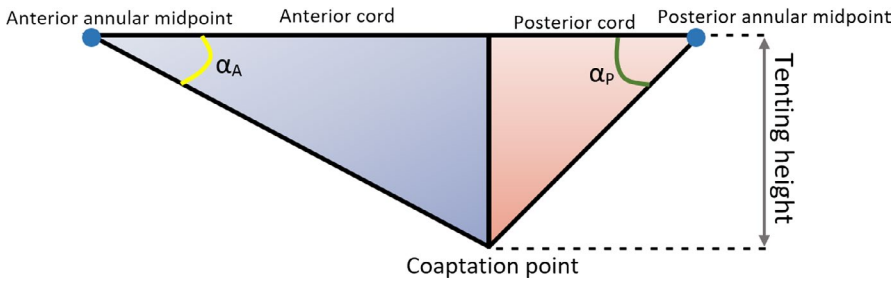


FIGURE 7 Coaptation triangle. The tenting height divides the base of the triangle (AP diameter) into two segments—the anterior and the posterior cords. α_A , anterior leaflet angle; α_P , posterior leaflet angle

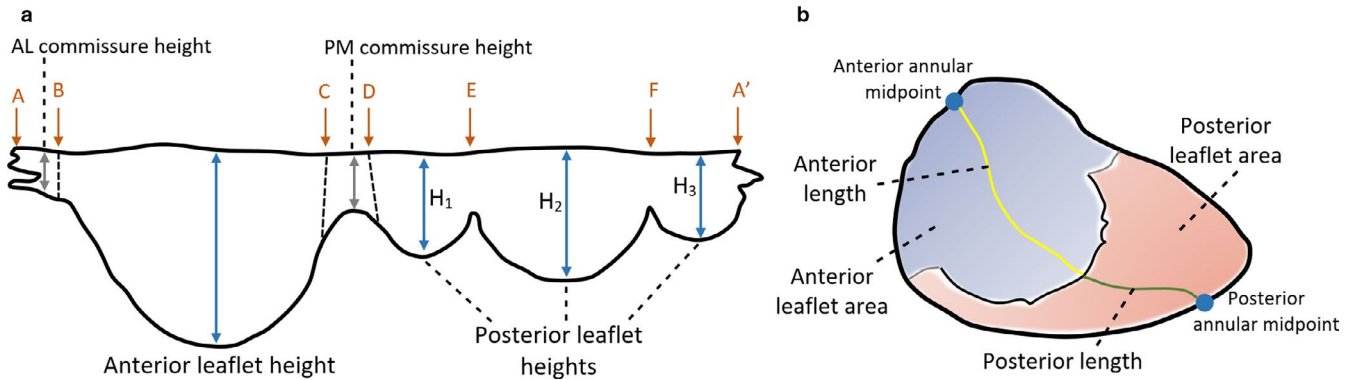


FIGURE 8 Parameters of human MV leaflet geometry, with an extended (a) and closed (b) leaflet representation. A-B, anterolateral commissure; B-C, anterior leaflet; C-D, posteromedial commissure; D-A', posterior leaflet; D-E, posteromedial commissural scallop (P1); E-F, middle scallop (P2); F-A', anterolateral commissural scallop (P3)

where A_{LA} is the anterior leaflet surface area (in mm^2) and the A_C is in mm,

$$A_{LA} = 114.830 + 10.630 \cdot A_C, \quad (24)$$

where the A_{AC} is in mm and the A_{LA} is in mm^2 ,

$$\delta = 17.840 + 0.150 \cdot A_{LA}, \quad (25)$$

where the A_{LA} is in mm^2 and δ is in mm (Duplessis and Marchand, 1964).

Similarly, further human ex vivo correlations between the posterior leaflet surface area and other dimensions of the valve were obtained from Duplessis and Marchand (1964): good associations with the A_C (Equation 26, $R^2 = .85$, p -value < .01) and P_{AC} (Equation 27,

$R^2 = .82$, p -value < .01) and a moderate association with the free edge length (Equation 28, $R^2 = .75$, p -value < .01):

$$P_{LA} = 65.749 + 4.262 \cdot A_C, \quad (26)$$

where P_{LA} is the posterior leaflet surface area (in mm^2) and the A_C is in mm,

$$P_{LA} = 113.250 + 5.798 \cdot P_{AC}, \quad (27)$$

where the P_{AC} is in mm and the P_{LA} is in mm^2 ,

$$\delta = 14.797 + 0.152 \cdot P_{LA}, \quad (28)$$

where the P_{LA} is in mm^2 and δ is in mm (Duplessis and Marchand, 1964).

In addition, a moderate correlation between anterior and posterior leaflet surface areas was also discovered from the data of Duplessis and Marchand (1964) (Equation 29, $R^2 = .71$, p -value $< .01$):

$$P_{LA} = 53.285 + 0.914 \cdot A_{LA}, \quad (29)$$

where the A_{LA} and P_{LA} are in mm^2 (Duplessis and Marchand, 1964).

The posterior leaflet has been mathematically characterised as a continuous shape around the annulus, with (Stevanella *et al.*, 2009; 2011; Choi *et al.*, 2016) or without (Kunzelman *et al.*, 1993; Cochran and Kunzelman, 1998; Kunzelman *et al.*, 2007; Domenichini and Pedrizzetti, 2015) scallop indentations. The main focus has been given to the mathematical definition of the complete leaflets' free margin. This has been generated through mathematical harmonic functions (Stevanella *et al.*, 2009), spline functions (Stevanella *et al.*, 2011) and parametric equations (Domenichini and Pedrizzetti, 2015). However, these frameworks simplify leaflet shape to great extent, resulting in overly idealised geometries.

Better leaflet geometrical descriptions have recently been developed. Khalighi *et al.* (2018) built high-quality 3D parametric models of MV leaflet surfaces using *ex vivo* high-resolution images from ovine MV, obtained through micro-computed tomography. They then employed quadric surfaces representing toroidal topology to create parametric large-scale models of the MV and information on the deviation between parameterised models and the original geometries to derive local thickness of leaflets (Khalighi *et al.*, 2018). Another study focused on the development of *ex vivo* methods to inform on the sensitivity of model performance to the accuracy of the input geometry and to acquire comprehensive datasets against which to validate computational simulations (Bloodworth *et al.*, 2017). These works could potentially be employed on high-fidelity MV models concerning healthy, diseased and repair states; however, as they rely on images obtained through an *ex vivo* imaging modality, translation to the generation of *in vivo* human MV models remains challenging.

3.4 | Papillary muscle position and chordae insertion

The human PMs exhibit great morphological variability (Stevanella *et al.*, 2009; 2011). Although two in number (Al-Atabi *et al.*, 2012), there are usually groups of muscles adjoining, reaching a total number as high as five and attaching to the left ventricular wall at its middle, upper or lower sections (Saha and Roy, 2018). Moreover, their shape is diversified, resembling either a cone (conical shape) or a elliptic paraboloid, having a truncated shape, or being bifurcated or trifurcated (Saha and Roy, 2018). Further, the number of chordae tendineae that attach to the PM, as well as their insertion distribution, is a source of variability. These features contribute to PM morphological heterogeneity, either in shape or attachment site. Therefore, current mathematical representations of the PM as unique points are restrictive and not accurately representative.

The PMs spatial position in humans has been mathematically defined, especially taking into account measurements such as their distance to the mitral annulus or to mitral coaptation (Sakai *et al.*, 1999; Yamaura *et al.*, 2008). Other measures of interest, such as the distance between PM or the inter-PM angle, have also been employed to describe PM morphology (Figure 9). Some studies have provided measurements of the PM to five key annular sites named o'clock points (Figure 10) (Sakai *et al.*, 1999; Yamaura *et al.*, 2008). Here, each PM is associated with three distances to the annulus, allowing the description of the 3D spatial position of their tips if assumed to be a unique 3D point. More recently, another study has employed knowledge on similar measurements to build a high-resolution 3D magnetic resonance imaging apparatus, giving rise to high-quality 3D models of the whole human MV structure (Stephens *et al.*, 2017).

The mathematical description of human chordae tendineae remains challenging, due to the fact that their geometry is of difficult detection through common *in vivo* imaging modalities (Dal-Bianco and Levine, 2013; Khalighi *et al.*, 2017) and meaning that human *ex vivo* studies are the primary sources of knowledge regarding chordal anatomy. Chordae tendineae are distinguished by their morphological diversity in number, insertion points into the leaflets, thickness and branching patterns, as given by previous human *ex vivo* studies (Lam *et al.*, 1970; Gunnal *et al.*, 2015). Regarding human MVs, it is difficult to characterise the exact insertion points of chordae into the leaflets with the imaging techniques currently available (Yamaura *et al.*, 2008), and even the mathematical description of the location of insertion points into the PMs and into the mitral leaflets is based upon assumptions and the expertise of clinicians (Stevanella *et al.*, 2011).

In reality, for a human MV model representation, it is common mathematically to simplify the shape of the PMs, as well as chordae insertion patterns: some studies represent the PM tips as unique 3D points where all chordae insert, as previously mentioned (Cochran and Kunzelman, 1998; Stevanella *et al.*, 2009; Prot *et al.*, 2010; Rim *et al.*, 2013); others assume a parabola representing a 2D cut-section of the PM shape, but where all chordae still insert on the tip (Park *et al.*, 2019); and others still, assume them to have a spherical (Stevanella *et al.*, 2011; Wang and Sun, 2013) or C-shape (Choi *et al.*, 2016) (schematised in Figure 11) and create different insertion points for the chordae according to their classification.

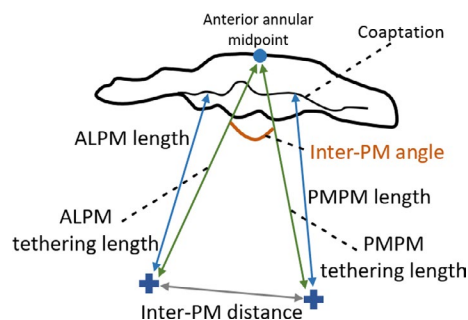


FIGURE 9 Measurements describing PM morphology. ALPM, anterolateral PM; PMPM, posteromedial PM

Recent studies based on ovine MV have looked into further characterising chordae tendineae geometry and topology (Khalighi *et al.*, 2017), as well as evaluating how native chordal anatomic characteristics affect valvular performance (Khalighi *et al.*, 2019). Khalighi *et al.* (2017) based their investigation on high-resolution micro-CT derived 3D models, obtaining mathematical descriptions of the chordae such as curve-skeleton characterisations, B-spline parameterisations and Reeb graph representations (see Figure 12). They used the curve-skeleton models to derive bifurcation and non-planarity angles and also analysed the spatial distribution of chordae insertion sites into the leaflets (Khalighi *et al.*, 2017). Their work yielded valuable information about chordal geometrical characterisation, including the presence of a non-homogeneous cross-sectional area along each segment (with chordal structure becoming thinner as it moves further away from the PM tip); the 2D nature of chordae, which collectively form a 3D load-bearing support structure of the MV leaflets; and the development of analytical statistical models that describe chordae geometry, as well as binary trees, which aid in the prediction of possible shapes for chordal structure (Khalighi *et al.*, 2017). Khalighi *et al.* (2019), on

the other hand, found that varying cross-sectional area, branching patterns and PM insertion points at the same origin did not greatly impact on ovine MV performance and they described an optimal chordae number range for appropriate function which eliminated over 75% of the native population of chordal insertions. Both studies then shed light on chordae tendineae geometrical characterisations which might possibly be applied to develop human MV models with simplified sub-apparatus structures as a mean to overcome the current issues with in vivo imaging modalities.

4 | CHANGES IN MITRAL VALVE MORPHOMETRY: DISEASE

4.1 | Carpentier's functional classification of MV disease

One of the most commonly used classifications of MV disease was designed by Carpentier (1983), sometimes referred to as the

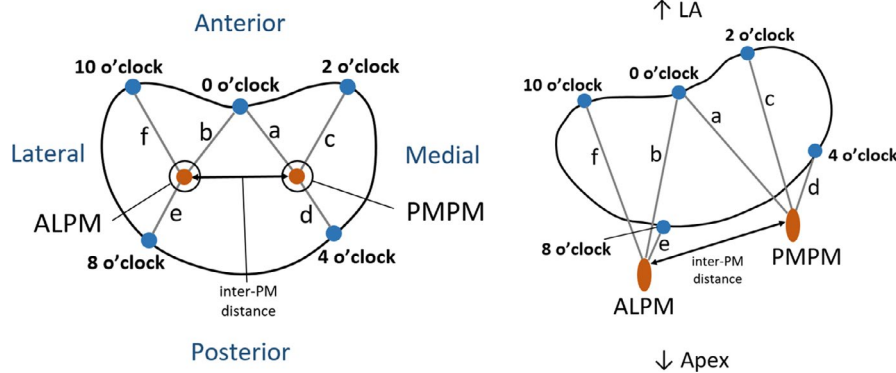


FIGURE 10 Distances between PM tips and o'clock points of mitral annulus, in axial (left) and isometric (right) views (adapted from Sakai *et al.*, 1999; Yamaura *et al.*, 2008). ALPM, anterolateral PM; PMPM, posteromedial PM; 0 o'clock, midpoint of the anterior annular circumference; 2 o'clock, right trigone; 10 o'clock, left trigone; 4 o'clock, separation of posterior and middle scallops of posterior leaflet; 8 o'clock, separation of anterior and middle scallops of posterior leaflet

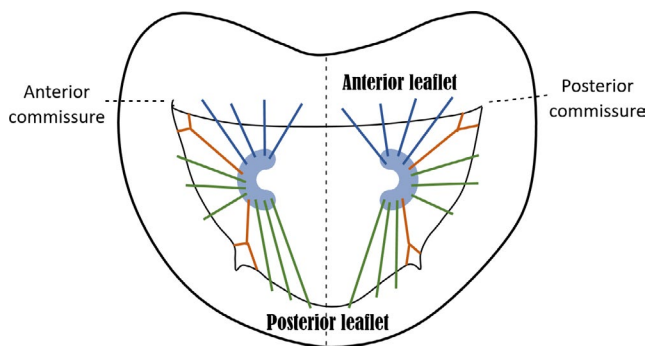


FIGURE 11 Axial view of C-shape representation for the PMs, as present in the literature and suggested by expert surgeons, as well as a simplified depiction of chordae tendineae insertion patterns. Blue, green and orange chordae are those inserting into the anterior leaflet, posterior leaflet and paracommissural zones, respectively

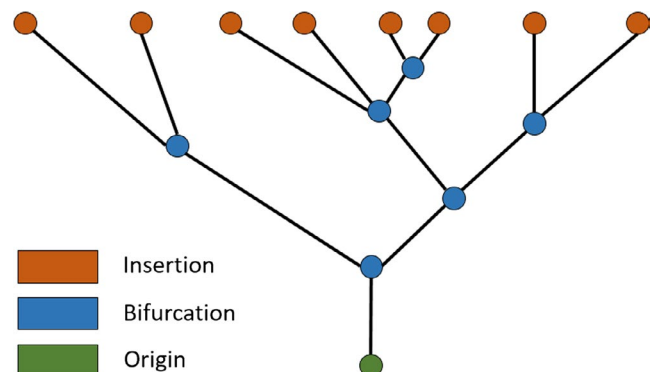


FIGURE 12 Example of Reeb graph employed to characterise chordae tendineae topology in Khalighi *et al.* (2017), illustrating the connectivity between branches. Green, blue and orange vertices correspond to chordal origin (at the PM level), bifurcation points and insertion points into the leaflets, respectively

'pathophysiologic triad' (Carpentier *et al.*, 1980). It divides MV dysfunctions into three categories, all of which yield lesions that lead to clinical mitral regurgitation. These categories are based on the position of leaflet margins with respect to the mitral annulus plane: type I refers to normal leaflet motion and is associated with annular dilation and leaflet perforation; type II characterises excessive leaflet motion, usually derived from elongation or rupture of the chordae tendineae and/or the PM; and type III relates to restricted leaflet motion due to retraction of the subvalvular apparatus (IIla) or PM displacement and left ventricular dilation, causing apical displacement (tethering) of the PM (IIlb). Further information on this classification and the associated lesions can be found elsewhere (Carpentier, 1983; Castillo *et al.*, 2011; Stone *et al.*, 2015). Mathematical interpretations of this classification were attempted in previous studies, for example representing annular dilation by increasing its diameter or PM displacement by increasing inter-PM distance (Park *et al.*, 2019). Taking this and the current literature available into account, examples of clinical lesions related to MV dysfunctional categories, and their influence in MV geometrical changes, are included in the following sections.

4.2 | Geometrical changes in the mitral annulus are linked to type I dysfunction

In type I dysfunction, the human mitral annulus undergoes structural changes, becoming larger and flatter and losing its saddle shape (Mihaila *et al.*, 2013; Lee *et al.*, 2017). A mathematical representation of this is shown in Figure 13, where the annulus was obtained using dimensions characteristic of annular dilation, including a lower AHCWR, displayed against a healthy configuration.

The increase in annular size associated with this type of mitral dysfunction compromises leaflet coaptation length and therefore prevents proper valve closing (Silbiger, 2011). For example, a previous *in vitro* study based on porcine MV showed that increasing annular area values (annular dilation) were associated with a decrease in the pressures needed to cause MV failure (Espino *et al.*, 2007). The association between the effective regurgitant orifice area (EROA) and MV geometry serves as a validation of the role played by abnormalities in shape in dysfunctional cases. Concerning

the human MV, increases in this index, linked to greater severity of regurgitation, have been associated with increasing annular circumference and area at end-systole, although such associations were poorly correlated ($R^2 = .38$, $R^2 = .48$, respectively, with p -value $< .01$) (Cong *et al.*, 2018). Lee *et al.* (2013) have also found an inverse correlation between EROA and AHCWR in the same time frame, showing loss of MV saddle shape with increasing regurgitation ($R^2 = .44$, p -value $< .01$) (Lee *et al.*, 2013).

Other clinical studies have also correlated an increase in EROA with greater non-coaptation distance between leaflets (maximal distance between both leaflet edges) at end-systole, as given by Equation (30) ($R^2 = .68$, p -value $< .01$) (Senechal *et al.*, 2012):

$$\lambda = 0.066 \cdot e^{(0.325 \cdot \mu)}, \quad (30)$$

where μ represents the non-coaptation distance (in mm) and λ represents the EROA (in cm^2).

In vivo human studies show that the flattening in MV shape present in disease is associated with loss of non-planarity (Silbiger, 2011; Lee *et al.*, 2013), quantified by increased NPAs (Mihaila *et al.*, 2013) and greater billowing, shown as a correlation between lower AHCWR and higher values of billow volume ($R^2 = .66$, p -value $< .01$) obtained at end-systole:

$$BV = 10.000 - 0.792 \cdot \varepsilon + 0.016 \cdot \varepsilon^2, \quad (31)$$

where BV represented the billow volume (ml) and ε represents the AHCWR (as a percentage) (Lee *et al.*, 2013).

In vivo studies have also shown a change in individual measurements describing annular shape in diseased cases: the AP diameter has been shown to increase in regurgitant valves (Lee *et al.*, 2013; Mihaila *et al.*, 2013), as well as the AL-PM diameter (Mihaila *et al.*, 2013) and the commissural width (Lee *et al.*, 2013). In addition, greater values of the circularity index are present in cases of regurgitation (Lee *et al.*, 2013), associated with loss of contractility for the MV and a more dominant circular configuration through the cardiac cycle. All these associations show that abnormal human mitral geometry is intrinsically linked to mitral regurgitation (Sonne *et al.*, 2009; Dal-Bianco and Levine, 2013; Lee *et al.*, 2013; Mihaila *et al.*, 2013).

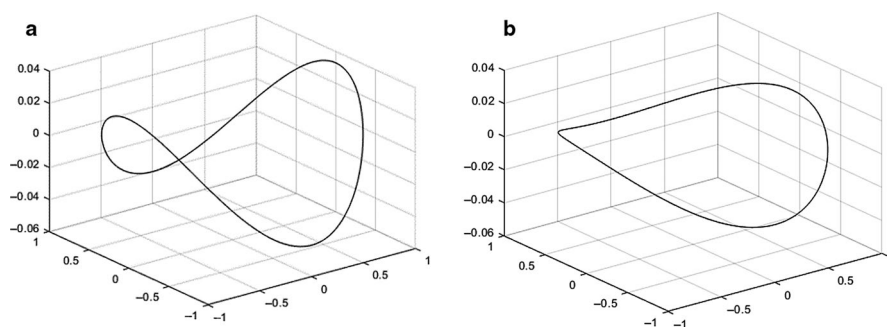


FIGURE 13 Hyperboloids representing: (a) a mitral annular normal saddle configuration; (b) a configuration associated with type I dysfunction, defined as in Park *et al.* (2019). The first configuration was created with the dimensions shown on Figure 6 and the diseased configuration on literature values for CW (42.2 mm), AP diameter (38.8 mm), AL-PM diameter (39 mm) and AHCWR (.132)

The process of annular dilation differs for anterior and posterior circumferences in the human MV, with the anterior fibrous portion being less prone to dilation (McCarthy *et al.*, 2010). Mathematically, this means that the inter-trigonal distance is not expected to change with mitral annular dilation (Suri *et al.*, 2009; Calleja *et al.*, 2015). The remaining 2/3 of the annulus (posterior annulus) is mainly muscular, dilating more easily (McCarthy *et al.*, 2010). The anterior and posterior leaflet surface areas also increase with mitral regurgitation (Senechal *et al.*, 2012; Dal-Bianco and Levine, 2013; Lee *et al.*, 2013; Mihaila *et al.*, 2013); however, no apparent trend in dilation concerning anterior vs posterior is present in the literature.

4.3 | Geometrical changes in the subvalvular apparatus are related to type III dysfunction

Configurational changes of the subvalvular apparatus have a profound impact on MV function. A previous *in vitro* study using porcine specimens assessed the effect of different annulo-papillary lengths in MV coaptation, with different lengths leading to different MV states: not only are increased values associated with damage to the valve, but a shortening in annulo-papillary lengths also induces diseased states (leaflet prolapse) (Espino *et al.*, 2007). An optimum annulo-papillary length is therefore needed for proper MV coaptation. In fact, type III dysfunctions of the MV have been associated with geometrical alterations of the subvalvular apparatus. Clinical studies have shown that the PMs suffer displacement in an attempt to attenuate the regurgitation effects (Silbiger, 2011; Lee *et al.*, 2013); this is translated into increased inter-PM distance (Kim *et al.*, 2014; Obase *et al.*, 2016), which has been well correlated with increased regurgitant volume in patients with severe functional ischaemic mitral regurgitation, as mathematically described by the equation below for end-systolic data ($R^2 = .84$, p -value < .01):

$$RV = -36.440 + 1.434 \cdot v, \quad (32)$$

where RV represents the regurgitant volume (in ml) and v represents the inter-PM distance (in mm) (Jensen *et al.*, 2010).

Type III dysfunction is also associated with increased left ventricular dimensions, which cause apical displacement of the PM. This leads to increased annulo-papillary lengths and chordae tendineae elongation (Obase *et al.*, 2016). Previous clinical studies have connected PM displacement with the severity of mitral regurgitation: increased apical displacement of the posteromedial PM (PMPM) was associated with greater regurgitant volume (Jensen *et al.*, 2010) and augmented tethering distance, characteristic of PM displacement, was correlated with an increasing mitral regurgitation fraction at mid-systole (Equation 33, R^2 stated as .64, p -value < .01) (Uemura *et al.*, 2005):

$$M_{RF} = -60.990 + 3.583 \cdot TD, \quad (33)$$

where TD represents the PMPM tethering distance (in mm^2) and M_{RF} represents the mitral regurgitation fraction (as a percentage).

Another clinical study found independent associations between apical displacement of the PMPM and posterior displacement of the AL-PM with increasing tenting area, related to loss of systolic annular function and regurgitation (Yiu *et al.*, 2000). However, the obtained data were too disperse to yield strong correlations among these parameters.

5 | FUTURE DIRECTIONS AND RECOMMENDATIONS FOR THE USE OF MORPHOMETRIC INFORMATION IN MITRAL VALVE CLINICAL ANALYSIS

This review paper focuses on grouping and briefly outlining the current best knowledge regarding MV morphometry by obtaining data from a range of different sources, including *in vitro*, *in vivo* and *in silico* studies. The quantitative data available have been analysed to derive further empirical mathematical relationships between dimensions. These can prove valuable to describe a healthy status of the MV, or to show the association between an abnormal valve shape and cases of dysfunction. It remains challenging to combine the morphometric information available in the literature to produce a coherent morphometric model of the human MV, based on mathematical correlations. Empirical relationships derived from direct correlations between dimensions and any relationships predicted analytically (or mathematically derived shapes) present with inherent differences. In addition, such correlations are derived from a specific imaging time frame, making it difficult to generalise these findings to the entire cardiac cycle.

Moreover, the use of different imaging modalities to obtain quantitative measurements, or the employment of different reference points, coordinate systems and anatomical landmarks, may lead to differing ranges for the same dimensions across studies. On the other hand, several imaging modalities present with a lack of spatial resolution, therefore making it difficult accurately to measure valve dimensions. It also remains challenging to represent the subvalvular apparatus rigorously, as current *in vivo* imaging modalities are unable to capture the chordae and PM properly. This is the motivation behind the use of *ex vivo* data in computational models, as well as complete *ex vivo* animal geometries, which, in combination with micro-CT imaging, allow for high-resolution detail of all MV components (Bloodworth *et al.*, 2017; Khalighi *et al.*, 2017; 2018).

Computational modelling has been directed towards the study of MV function: while some studies have focused on normal physiological valve functioning (Votta *et al.*, 2008; Wang and Sun, 2013; Domenichini and Pedrizzetti, 2015; Gao *et al.*, 2017a), others have focused on diseased cases (Wenk *et al.*, 2010; Rim *et al.*, 2013; Choi *et al.*, 2016) and surgical procedures (Ge *et al.*, 2014; Rim *et al.*, 2015; Rausch *et al.*, 2017). The first geometrical models were based on idealised shapes of the MV, derived from literature data (Kunzelman *et al.*, 1993; Salgo *et al.*, 2002). However, as the accuracy of MV models is highly sensitive to valve geometry, patient-specific approaches

have been preferred, with the MV apparatus being derived from medical images (Rim *et al.*, 2013; Ge *et al.*, 2014). Moreover, studies have been focused on less invasive methodologies for the determination of mitral tissue properties in vivo, including leaflet strains (Rego *et al.*, 2018). Faster and more efficient methods to study MV function are becoming a reality; for example, a recent study employed a complete human heart model (Baillargeon *et al.*, 2014) to study ventricular dilation, its impact on the MV structure and its repair through annuloplasty (Rausch *et al.*, 2017). This demonstrates the great potential of computational simulations to optimise medical intervention, develop tailored device designs and aid in treatment management. The use of a more complete set of morphometric information on the MV, such as the one described in this paper, may aid in this endeavour, which can then be useful for studying the biomechanics associated with specific valve shapes in healthy and diseased ranges.

CONFLICT OF INTEREST

None.

AUTHOR CONTRIBUTIONS

All authors were involved in the design of the study and have critically revised the manuscript. Individual contributions are as follows: Miss Diana Oliveira: Initial draft of the manuscript; gathering of morphometric mitral valve information from the current literature, for healthy and diseased cases; statistical analysis with published data; acquisition of mitral valve anatomic data and respective data analysis. Dr Janaki Srinivasan: Acquisition of mitral valve anatomic data. Dr Dana Dawson: Clinical guidance; recommendation of the clinical database to employ and decision on which sample to use. Dr Keith Buchan: Surgical guidance; determination of relevant morphometric aspects of the mitral valve, including anatomic arrangements from the surgical point of view; advice on image sketches for the manuscript. Dr Daniel Espino: Guidance on organisation and presentation of information and data. Prof Duncan Shepherd: Guidance on organisation and presentation of information and data.

ETHICAL APPROVAL

The data obtained by the authors are for healthy volunteers recruited under the ethically approved research study 'Exercise Capacity in Adults' with REC reference 13/NS/0034 and IRAS ID 127501.

ORCID

Diana Oliveira  <https://orcid.org/0000-0002-8151-1333>

REFERENCES

- Al-Atabi, M., Espino, D.M., Hukins, D.W. and Buchan, K.G. (2012) Biomechanical assessment of surgical repair of the mitral valve. Proceedings of the Institution of Mechanical Engineers. Part H. *Journal of Engineering in Medicine*, 226, 275–287.
- Baillargeon, B., Rebelo, N., Fox, D.D., Taylor, R.L. and Kuhl, E. (2014) The Living Heart Project: a robust and integrative simulator for human heart function. *European Journal of Mechanics - A/Solids*, 48, 38–47.
- Bloodworth, C.H.T., Pierce, E.L., Easley, T.F., Drach, A., Khalighi, A.H., Toma, M., et al. (2017) Ex vivo methods for informing computational models of the mitral valve. *Annals of Biomedical Engineering*, 45, 496–507.
- Bouma, W. and Gorman, R.C. (2019) Commentary: Three-dimensional P3 tethering angle at the heart of future surgical decision making in ischemic mitral regurgitation. *Journal of Thoracic and Cardiovascular Surgery*, 157, 1806–1807.
- Calleja, A., Poulin, F., Woo, A., Meineri, M., Jedrzkiewicz, S., Vannan, M.A., et al. (2015) Quantitative modeling of the mitral valve by three-dimensional transesophageal echocardiography in patients undergoing mitral valve repair: correlation with intraoperative surgical technique. *Journal of the American Society of Echocardiography*, 28, 1083–1092.
- Carpentier, A. (1983) Cardiac valve surgery—the 'French correction'. *Journal of Thoracic and Cardiovascular Surgery*, 86, 323–337.
- Carpentier, A., Chauvaud, S., Fabiani, J.N., Deloche, A., Relland, J., Lessana, A., et al. (1980) Reconstructive surgery of mitral valve incompetence: ten-year appraisal. *Journal of Thoracic and Cardiovascular Surgery*, 79, 338–348.
- Carpentier, A.F., Lessana, A., Relland, J.Y., Belli, E., Mihaileanu, S., Berrebi, A.J., et al. (1995) The 'physio-ring': an advanced concept in mitral valve annuloplasty. *Annals of Thoracic Surgery*, 60, 1177–1185; discussion 1185–1186.
- Castillo, J.G., Solis, J., Gonzalez-Pinto, A. and Adams, D.H. (2011) Surgical echocardiography of the mitral valve. *Revista Espanola de Cardiologia*, 64, 1169–1181.
- Choi, A., McPherson, D.D. and Kim, H. (2016) Biomechanical evaluation of the pathophysiologic developmental mechanisms of mitral valve prolapse: effect of valvular morphologic alteration. *Medical & Biological Engineering & Computing*, 54, 799–809.
- Ciarka, A., Braun, J., Delgado, V., Versteegh, M., Boersma, E., Klautz, R., et al. (2010) Predictors of mitral regurgitation recurrence in patients with heart failure undergoing mitral valve annuloplasty. *American Journal of Cardiology*, 106, 395–401.
- Cochran, R.P. and Kunzelman, K.S. (1998) Effect of papillary muscle position on mitral valve function: relationship to homografts. *Annals of Thoracic Surgery*, 66, S155–S161.
- Cong, T., Gu, J., Lee, A.P., Shang, Z., Sun, Y., Sun, Q., et al. (2018) Quantitative analysis of mitral valve morphology in atrial functional mitral regurgitation using real-time 3-dimensional echocardiography atrial functional mitral regurgitation. *Cardiovascular Ultrasound*, 16, 13.
- Dal-Bianco, J.P. and Levine, R.A. (2013) Anatomy of the mitral valve apparatus: role of 2D and 3D echocardiography. *Cardiology Clinics*, 31, 151–164.
- Delgado, V., Tops, L.F., Schuijf, J.D., de Roos, A., Brugada, J., Schalij, M.J., et al. (2009) Assessment of mitral valve anatomy and geometry with multislice computed tomography. *JACC: Cardiovascular Imaging*, 2, 556–565.
- Deorsola, L. and Bellone, A. (2018) Coaptation Triangle and Golden Proportion in mitral valve anatomy. Does nature play with geometry? *Echocardiography*, 35, 30–38.
- Domenichini, F. and Pedrizzetti, G. (2015) Asymptotic model of fluid-tissue interaction for mitral valve dynamics. *Cardiovascular Engineering and Technology*, 6, 95–104.
- Dudzinski, D.M. and Hung, J. (2014) Echocardiographic assessment of ischemic mitral regurgitation. *Cardiovascular Ultrasound*, 12, 46.
- Duplessis, L.A. and Marchand, P. (1964) The anatomy of the mitral valve and its associated structures. *Thorax*, 19, 221–227.
- Eckert, C.E., Zubiato, B., Vergnat, M., Gorman, J.H., 3rd, Gorman, R.C. and Sacks, M.S. (2009) In vivo dynamic deformation of the mitral valve annulus. *Annals of Biomedical Engineering*, 37, 1757–1771.
- Espino, D.M., Shepherd, D.E., Hukins, D.W. and Buchan, K.G. (2005) The role of Chordae tendineae in mitral valve competence. *Journal of Heart Valve Disease*, 14, 603–609.

- Espino, D.M., Shepherd, D.E. and Buchan, K.G. (2007) Effect of mitral valve geometry on valve competence. *Heart and Vessels*, 22, 109–115.
- Gao, H., Feng, L., Qi, N., Berry, C., Griffith, B.E. and Luo, X. (2017a) A coupled mitral valve-left ventricle model with fluid-structure interaction. *Medical Engineering & Physics*, 47, 128–136.
- Gao, H., Qi, N., Feng, L., Ma, X., Danton, M., Berry, C., et al. (2017b) Modelling mitral valvular dynamics-current trend and future directions. *International Journal for Numerical Methods in Biomedical Engineering*, 33, 33:e2858, 1–15.
- Garbi, M. and Monaghan, M.J. (2015) Quantitative mitral valve anatomy and pathology. *Echo Research and Practice*, 2, R63–72.
- Ge, L., Morrel, W.G., Ward, A., Mishra, R., Zhang, Z., Guccione, J.M., et al. (2014) Measurement of mitral leaflet and annular geometry and stress after repair of posterior leaflet prolapse: virtual repair using a patient-specific finite element simulation. *Annals of Thoracic Surgery*, 97, 1496–1503.
- Grbic, S., Easley, T.F., Mansi, T., Bloodworth, C.H., Pierce, E.L., Voigt, I., et al. (2017) Personalized mitral valve closure computation and uncertainty analysis from 3D echocardiography. *Medical Image Analysis*, 35, 238–249.
- Gunnal, S.A., Wabale, R.N. and Farooqui, M.S. (2015) Morphological study of chordae tendinae in human cadaveric hearts. *Heart Views*, 16, 1–12.
- Hirakawa, S., Sasayama, S., Tomoike, H., Crozatier, B., Franklin, D., McKown, D., et al. (1977) In situ measurement of papillary muscle dynamics in the dog left ventricle. *American Journal of Physiology*, 233, H384–H391.
- Ionasec, R.I., Voigt, I., Georgescu, B., Wang, Y., Houle, H., Vega-Higuera, F., et al. (2010) Patient-specific modeling and quantification of the aortic and mitral valves from 4-D cardiac CT and TEE. *IEEE Transactions on Medical Imaging*, 29, 1636–1651.
- Jassar, A.S., Vergnat, M., Jackson, B.M., McGarvey, J.R., Cheung, A.T., Ferrari, G., et al. (2014) Regional annular geometry in patients with mitral regurgitation: implications for annuloplasty ring selection. *Annals of Thoracic Surgery*, 97, 64–70.
- Jensen, H., Jensen, M.O., Smerup, M.H., Ringgaard, S., Sorensen, T.S., Andersen, N.T., et al. (2010) Three-dimensional assessment of papillary muscle displacement in a porcine model of ischemic mitral regurgitation. *Journal of Thoracic and Cardiovascular Surgery*, 140, 1312–1318.
- Jiang, L., Owais, K., Matyal, R., Khabbaz, K.R., Liu, D.C., Montealegre-Gallegos, M., et al. (2014) Dynamism of the mitral annulus: a spatial and temporal analysis. *Journal of Cardiothoracic and Vascular Anesthesia*, 28, 1191–1197.
- Jimenez, J.H., Liou, S.W., Padala, M., He, Z., Sacks, M., Gorman, R.C., et al. (2007) A saddle-shaped annulus reduces systolic strain on the central region of the mitral valve anterior leaflet. *Journal of Thoracic and Cardiovascular Surgery*, 134, 1562–1568.
- Jolley, M.A., Ghelani, S.J., Adar, A. and Harrild, D.M. (2017) Three-dimensional mitral valve morphology and age-related trends in children and young adults with structurally normal hearts using transthoracic echocardiography. *Journal of the American Society of Echocardiography*, 30, 561–571.
- Kaiser, A.D., McQueen, D.M. and Peskin, C.S. (2019) Modeling the mitral valve. *International Journal for Numerical Methods in Biomedical Engineering*, 35, e3240.
- Khalighi, A.H., Drach, A., Bloodworth, C.H.T., Pierce, E.L., Yoganathan, A.P., Gorman, R.C., et al. (2017) Mitral valve chordae tendineae: topological and geometrical characterization. *Annals of Biomedical Engineering*, 45, 378–393.
- Khalighi, A.H., Drach, A., Gorman, R.C., Gorman, J.H. 3rd and Sacks, M.S. (2018) Multi-resolution geometric modeling of the mitral heart valve leaflets. *Biomechanics and Modeling in Mechanobiology*, 17, 351–366.
- Khalighi, A.H., Rego, B.V., Drach, A., Gorman, R.C., Gorman, J.H. 3rd and Sacks, M.S. (2019) Development of a functionally equivalent model of the mitral valve chordae tendineae through topology optimization. *Annals of Biomedical Engineering*, 47, 60–74.
- Kim, K., Kaji, S., An, Y., Nishino, T., Tani, T., Kitai, T., et al. (2014) Interpapillary muscle distance independently affects severity of functional mitral regurgitation in patients with systolic left ventricular dysfunction. *Journal of Thoracic and Cardiovascular Surgery*, 148, 434–440e1.
- Kunzelman, K.S., Cochran, R.P., Chuong, C., Ring, W.S., Verrier, E.D. and Eberhart, R.D. (1993) Finite element analysis of the mitral valve. *Journal of Heart Valve Disease*, 2, 326–340.
- Kunzelman, K.S., Cochran, R.P., Verrier, E.D. and Eberhart, R.C. (1994) Anatomic basis for mitral valve modelling. *Journal of Heart Valve Disease*, 3, 491–496.
- Kunzelman, K.S., Einstein, D.R. and Cochran, R.P. (2007) Fluid-structure interaction models of the mitral valve: function in normal and pathological states. *Philosophical Transactions of the Royal Society of London. Series B, Biological Sciences*, 362, 1393–1406.
- Lam, J.H., Ranganathan, N., Wigle, E.D. and Silver, M.D. (1970) Morphology of the human mitral valve. I. Chordae tendineae: a new classification. *Circulation*, 41, 449–458.
- Lee, A.P., Hsiung, M.C., Salgo, I.S., Fang, F., Xie, J.M., Zhang, Y.C., et al. (2013) Quantitative analysis of mitral valve morphology in mitral valve prolapse with real-time 3-dimensional echocardiography: importance of annular saddle shape in the pathogenesis of mitral regurgitation. *Circulation*, 127, 832–841.
- Lee, A.P., Jin, C.N., Fan, Y., Wong, R.H.L., Underwood, M.J. and Wan, S. (2017) Functional implication of mitral annular disjunction in mitral valve prolapse: a quantitative dynamic 3D echocardiographic study. *JACC: Cardiovascular Imaging*, 10, 1424–1433.
- Levack, M.M., Jassar, A.S., Shang, E.K., Vergnat, M., Woo, Y.J., Acker, M.A., et al. (2012) Three-dimensional echocardiographic analysis of mitral annular dynamics: implication for annuloplasty selection. *Circulation*, 126, S183–S188.
- Lomholt, M., Nielsen, S.L., Hansen, S.B., Andersen, N.T. and Hasenkam, J.M. (2002) Differential tension between secondary and primary mitral chordae in an acute in-vivo porcine model. *Journal of Heart Valve Disease*, 11, 337–345.
- Machino-Ohtsuka, T., Seo, Y., Ishizu, T., Sato, K., Sugano, A., Yamamoto, M., et al. (2016) Novel mechanistic insights into atrial functional mitral regurgitation—3-dimensional echocardiographic study. *Circulation Journal*, 80, 2240–2248.
- Mansi, T., Voigt, I., Georgescu, B., Zheng, X., Mengue, E.A., Hackl, M., et al. (2012) An integrated framework for finite-element modeling of mitral valve biomechanics from medical images: application to MitralClip intervention planning. *Medical Image Analysis*, 16, 1330–1346.
- Marzilli, M., Sabbah, H.N., Lee, T. and Stein, P.D. (1980) Role of the papillary muscle in opening and closure of the mitral valve. *American Journal of Physiology*, 238, H348–H354.
- McCarthy, K.P., Ring, L. and Rana, B.S. (2010) Anatomy of the mitral valve: understanding the mitral valve complex in mitral regurgitation. *European Journal of Echocardiography*, 11, i3–9.
- Mihaila, S., Muraru, D., Casablana, S., Peluso, D., Cucchini, U., del Bianco, L., et al. (2013) Three-dimensional changes in mitral valve annulus geometry in organic and functional mitral regurgitation: insights for mitral valve repair. *European Heart Journal*, 34, 4751.
- Nielsen, S.L., Timek, T.A., Green, G.R., Dagum, P., Daughters, G.T., Hasenkam, J.M., et al. (2003) Influence of anterior mitral leaflet second-order chordae tendineae on left ventricular systolic function. *Circulation*, 108, 486–491.
- Obase, K., Weinert, L., Hollatz, A., Farooqui, F., Roberts, J.D., Minhaj, M.M., et al. (2016) Elongation of chordae tendineae as an adaptive process to reduce mitral regurgitation in functional mitral regurgitation. *European Heart Journal of Cardiovascular Imaging*, 17, 500–509.

- Okamoto, H., Itoh, Y. and Nara, Y. (2007) Geometric analysis of the anterior mitral leaflet and mitral valve orifice in cadaveric hearts. *Circulation Journal*, 71, 1794–1799.
- Owais, K., Montealegre-Gallegos, M., Jeganathan, J., Matyal, R., Khabbaz, K.R. and Mahmood, F. (2016) Dynamic changes in the ischemic mitral annulus: implications for ring sizing. *Annals of Cardiac Anaesthesia*, 19, 15–19.
- Padala, M., Sacks, M.S., Liou, S.W., Balachandran, K., He, Z. and Yoganathan, A.P. (2010) Mechanics of the mitral valve strut chordae insertion region. *Journal of Biomechanical Engineering*, 132, 081004.
- Park, J., Geirsson, A. and Bonde, P.N. (2019) Mathematical blueprint of a mitral valve. *Seminars in Thoracic and Cardiovascular Surgery*, 31, 399–411.
- Pouch, A.M., Vergnat, M., McGarvey, J.R., Ferrari, G., Jackson, B.M., Sehgal, C.M., et al. (2014) Statistical assessment of normal mitral annular geometry using automated three-dimensional echocardiographic analysis. *Annals of Thoracic Surgery*, 97, 71–77.
- Prot, V., Skallerud, B., Sommer, G. and Holzapfel, G.A. (2010) On modelling and analysis of healthy and pathological human mitral valves: two case studies. *Journal of the Mechanical Behavior of Biomedical Materials*, 3, 167–177.
- Ranganathan, N., Lam, J.H., Wigle, E.D. and Silver, M.D. (1970) Morphology of the human mitral valve. II. The valve leaflets. *Circulation*, 41, 459–467.
- Rausch, M.K., Bothe, W., Kvitting, J.P., Swanson, J.C., Ingels, N.B. Jr., Miller, D.C., et al. (2011) Characterization of mitral valve annular dynamics in the beating heart. *Annals of Biomedical Engineering*, 39, 1690–1702.
- Rausch, M.K., Zollner, A.M., Genet, M., Baillargeon, B., Bothe, W. and Kuhl, E. (2017) A virtual sizing tool for mitral valve annuloplasty. *International Journal for Numerical Methods in Biomedical Engineering*, 33, 33:e02788, 1–14.
- Rego, B.V., Khalighi, A.H., Drach, A., Lai, E.K., Pouch, A.M., Gorman, R.C., et al. (2018) A noninvasive method for the determination of in vivo mitral valve leaflet strains. *International Journal for Numerical Methods in Biomedical Engineering*, 34, e3142.
- Rim, Y., Choi, A., McPherson, D.D. and Kim, H. (2015) Personalized computational modeling of mitral valve prolapse: virtual leaflet resection. *PLoS ONE*, 10, e0130906.
- Rim, Y., McPherson, D.D., Chandran, K.B. and Kim, H. (2013) The effect of patient-specific annular motion on dynamic simulation of mitral valve function. *Journal of Biomechanics*, 46, 1104–1112.
- Saha, A. and Roy, S. (2018) Papillary muscles of left ventricle—Morphological variations and its clinical relevance. *Indian Heart Journal*, 70, 894–900.
- Sakai, T., Okita, Y., Ueda, Y., Tahata, T., Ogino, H., Matsuyama, K., et al. (1999) Distance between mitral annulus and papillary muscles: anatomic study in normal human hearts. *Journal of Thoracic and Cardiovascular Surgery*, 118, 636–641.
- Salgo, I.S., Gorman, J.H. 3rd, Gorman, R.C., Jackson, B.M., Bowen, F.W., Plappert, T., et al. (2002) Effect of annular shape on leaflet curvature in reducing mitral leaflet stress. *Circulation*, 106, 711–717.
- Sedransk, K.L., Grande-Allen, K.J. and Vesely, I. (2002) Failure mechanics of mitral valve chordae tendineae. *Journal of Heart Valve Disease*, 11, 644–650.
- Senechal, M., Michaud, N., Machaalany, J., Bernier, M., Dubois, M., Magne, J., et al. (2012) Relation of mitral valve morphology and motion to mitral regurgitation severity in patients with mitral valve prolapse. *Cardiovasc Ultrasound*, 10, 3.
- Shen, X., Wang, T., Cao, X. and Cai, L. (2017) The geometric model of the human mitral valve. *PLoS ONE*, 12, e0183362.
- Silbiger, J.J. (2011) Mechanistic insights into ischemic mitral regurgitation: echocardiographic and surgical implications. *Journal of the American Society of Echocardiography*, 24, 707–719.
- Sonne, C., Sugeng, L., Watanabe, N., Weinert, L., Saito, K., Tsukiji, M., et al. (2009) Age and body surface area dependency of mitral valve and papillary apparatus parameters: assessment by real-time three-dimensional echocardiography. *European Journal of Echocardiography*, 10, 287–294.
- Stephens, S.E., Liachenko, S., Ingels, N.B., Wenk, J.F. and Jensen, M.O. (2017) High resolution imaging of the mitral valve in the natural state with 7 Tesla MRI. *PLoS ONE*, 12, e0184042.
- Stevanella, M., Votta, E. and Redaelli, A. (2009) Mitral valve finite element modeling: implications of tissues' nonlinear response and annular motion. *Journal of Biomechanical Engineering*, 131, 121010.
- Stevanella, M., Maffessanti, F., Conti, C.A., Votta, E., Arnoldi, A., Lombardi, M., et al. (2011) Mitral valve patient-specific finite element modeling from cardiac MRI: application to an annuloplasty procedure. *Cardiovascular Engineering and Technology*, 2, 66–76.
- Stone, G.W., Vahanian, A.S., Adams, D.H., Abraham, W.T., Borer, J.S., Bax, J.J., et al. (2015) Clinical trial design principles and endpoint definitions for transcatheter mitral valve repair and replacement: part 1: clinical trial design principles: a consensus document from the Mitral Valve Academic Research Consortium. *Journal of the American College of Cardiology*, 66, 278–307.
- Sun, X., Jiang, Y., Huang, G., Huang, J., Shi, M., Pang, L., et al. (2019) Three-dimensional mitral valve structure in predicting moderate ischemic mitral regurgitation improvement after coronary artery bypass grafting. *Journal of Thoracic and Cardiovascular Surgery*, 157(1795–1803), e2.
- Suri, R.M., Grewal, J., Mankad, S., Enriquez-Sarano, M., Miller, F.A. Jr. and Schaff, H.V. (2009) Is the anterior intertrigonal distance increased in patients with mitral regurgitation due to leaflet prolapse? *Annals of Thoracic Surgery*, 88, 1202–1208.
- Tang, Z., Fan, Y.T., Wang, Y., Jin, C.N., Kwok, K.W. and Lee, A.P. (2019) Mitral annular and left ventricular dynamics in atrial functional mitral regurgitation: a three-dimensional and speckle-tracking echocardiographic study. *Journal of the American Society of Echocardiography*, 32, 503–513.
- Timek, T.A., Nielsen, S.L., Green, G.R., Dagum, P., Bolger, A.F., Daughters, G.T., et al. (2001) Influence of anterior mitral leaflet second-order chordae on leaflet dynamics and valve competence. *Annals of Thoracic Surgery*, 72, 535–540.
- Topilsky, Y., Vaturi, O., Watanabe, N., Bichara, V., Nkomo, V.T., Michelena, H., et al. (2013) Real-time 3-dimensional dynamics of functional mitral regurgitation: a prospective quantitative and mechanistic study. *Journal of the American Heart Association*, 2, e000039.
- Uemura, T., Otsuji, Y., Nakashiki, K., Yoshifuku, S., Maki, Y., Yu, B., et al. (2005) Papillary muscle dysfunction attenuates ischemic mitral regurgitation in patients with localized basal inferior left ventricular remodeling: insights from tissue Doppler strain imaging. *Journal of the American College of Cardiology*, 46, 113–119.
- Veronesi, F., Corsi, C., Sugeng, L., Mor-Avi, V., Caiani, E.G., Weinert, L., et al. (2009) A study of functional anatomy of aortic-mitral valve coupling using 3D matrix transesophageal echocardiography. *Circulation: Cardiovascular Imaging*, 2, 24–31.
- Votta, E., Caiani, E., Veronesi, F., Soncini, M., Montevecchi, F.M. and Redaelli, A. (2008) Mitral valve finite-element modelling from ultrasound data: a pilot study for a new approach to understand mitral function and clinical scenarios. *Philosophical Transactions. Series A, Mathematical, Physical, and Engineering Sciences*, 366, 3411–3434.
- Wang, Q. and Sun, W. (2013) Finite element modeling of mitral valve dynamic deformation using patient-specific multi-slices computed tomography scans. *Annals of Biomedical Engineering*, 41, 142–153.
- Warraich, H.J., Chaudary, B., Maslow, A., Panzica, P.J., Pugsley, J. and Mahmood, F. (2012) Mitral annular nonplanarity: correlation between annular height/commissural width ratio and the nonplanarity angle. *Journal of Cardiothoracic and Vascular Anesthesia*, 26, 186–190.
- Wenk, J.F., Zhang, Z., Cheng, G., Malhotra, D., Acevedo-Bolton, G., Burger, M., et al. (2010) First finite element model of the left ventricle

- with mitral valve: insights into ischemic mitral regurgitation. *Annals of Thoracic Surgery*, 89, 1546–1553.
- Wilcox, A.G., Buchan, K.G. and Espino, D.M. (2014) Frequency and diameter dependent viscoelastic properties of mitral valve chordae tendineae. *Journal of the Mechanical Behavior of Biomedical Materials*, 30, 186–195.
- Yamaura, Y., Watanabe, N., Ogasawara, Y., Tsukiji, M., Okahashi, N., Okura, H., et al. (2008) Three-dimensional echocardiographic measurements of distance between papillary muscles and mitral annulus: assessment with three-dimensional quantification software system. *Journal of Echocardiography*, 6, 67–73.
- Yiu, S.F., Enriquez-Sarano, M., Tribouilloy, C., Seward, J.B. and Tajik, A.J. (2000) Determinants of the degree of functional mitral regurgitation in patients with systolic left ventricular dysfunction: a quantitative clinical study. *Circulation*, 102, 1400–1406.
- Zhang, F., Kanik, J., Mansi, T., Voigt, I., Sharma, P., Ionasec, R.I., et al. (2017) Towards patient-specific modeling of mitral valve repair: 3D

transesophageal echocardiography-derived parameter estimation. *Medical Image Analysis*, 35, 599–609.

SUPPORTING INFORMATION

Additional supporting information may be found online in the Supporting Information section.

How to cite this article: Oliveira D, Srinivasan J, Espino D, Buchan K, Dawson D, Shepherd D. Geometric description for the anatomy of the mitral valve: A review. *J. Anat.* 2020;237:209–224. <https://doi.org/10.1111/joa.13196>